
Proceedings Paper:
Gurdal, O., Rae, B., Zonuzi, A. et al. (1 more author) (2020) Vision-assisted robotic finishing of friction stir-welded corner joints. In: Denkena, B., (ed.) Procedia Manufacturing. 19th Machining Innovations Conference for Aerospace Industry 2019 (MIC 2019), 27-28 Nov 2019, Garbsen, Germany. Elsevier BV , pp. 70-76.

https://doi.org/10.1016/j.promfg.2020.02.013

Available online at www.sciencedirect.com

ScienceDirect

Procedia Manufacturing 40 (2019) 70–76

Procedia MANUFACTURING

www.elsevier.com/locate/procedia

19th Machining Innovations Conference for Aerospace Industry 2019 (MIC 2019), November 27th - 28th 2019, Hannover, Germany

Vision-assisted robotic finishing of friction stir-welded corner joints

Ozan Gurdal[a], Benjamin Rae[a], Arman Zonuzi[a], Erdem Ozturk[b]*

[a]*Nuclear AMRC, University of Sheffield, Advanced Manufacturing Park, Brunel Way,Catcliffe, Rotherham, S60 5WG*
[b]*AMRC with Boeing, University of Sheffield, Advanced Manufacturing Park, Wallis Way, Catcliffe, Rotherham, S60 5TZ*

* Corresponding author. Tel.:+44-114-222-1747; *E-mail address:* e.ozturk@amrc.co.uk

Abstract

One required process in the fabrication of large components is welding, after which there may be a need for machining to achieve final dimensions and uniform surfaces. Friction stir-welding (FSW) is a typical example after which a series of deburring and grinding operations are carried out. Currently, the majority of these operations are carried out either manually, by human workers, or on machine tools which results in bottlenecks in the process flows. This paper presents a robotic finishing system to automate the finishing of friction stir-welded parts with minimum human involvement. In a sequence, the system can scan and reconstruct the 3D model of the part, localise it in the robot frame and generate a suitable machining path accordingly, to remove the excess material from FSW without violating process constraints. Results of the cutting trials carried out for demonstration have shown that the developed system can consistently machine the corner joints of an industrial scale part to desired surface quality which is around 1.25 μm in, R_a, the arithmetic average of the surface roughness.

Keywords: robotic machining; robotic deburring; vision-assisted machining

1. Introduction

Friction stir-welding is an effective solid-state joining technique especially suitable for aluminium alloys because it minimises the risk of common defects associated with fusion welding processes. Originally developed in 1991 by The Welding Institute (TWI) for aerospace applications, it has been also adopted by different industries including the marine, nuclear, automotive and rail for the fabrication of large components and joining of dissimilar materials [1]. Flash formation is inevitable in friction stir-welding due to the combination of friction-induced heat and high axial loads causing a part of the material around the joint line to be gradually extruded along the path that the welding pin traverses. Depending on the process parameters, the height of the generated flash could be up to a few centimetres which might be difficult to remove manually once it has cooled down. In addition to flash formation, it is also common that friction stir-welded surface is imprinted with the plunging and feed marks of the FSW tool during the operation. These two main issues require friction stir-welded components to be machined off in a subsequent operation which could be milling or manual finishing depending on the shape, size and cost of the component and also available machinery. Assuming that required technical specifications are met, conventional milling machines can carry out friction stir-welding when equipped with correct tooling and fixtures which is a cost-effective solution for small and medium enterprises. Fig. 1 (a) and (b) illustrate this process for an example component from the civil nuclear industry. The cycle time of weld finishing operations such as deflashing and deburring on the machine tool as shown in Fig. 1 (c) including the setup, programming and machining is comparable to that of the friction stir-welding. This is a major issue in terms of productivity, as it means that the machine tool

10.1016/j.promfg.2020.02.013

is allocated for a significantly lower value-added task instead of carrying out friction stir-welding or milling. Robots can be tasked with this kind of weld finishing operations which would release the machine tools and also enable the automation of additional operations, such as grinding and inspection, which are generally carried out to meet and ensure the final surface quality.

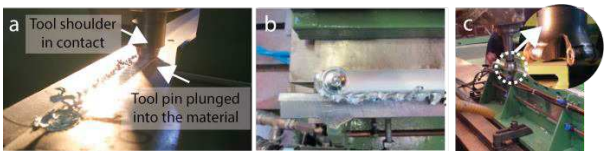

Fig. 1. (a) FSW probe during process. (b) Formation of flash and FSW marks. (c) Face-milling for initial deburring.

One of the fundamental studies on robotic weld finishing was carried out by Whitney et al. [2] who developed a force-controlled robotic disk grinding system to level down the weld bead, apparently, on planar surfaces. The system was also equipped with a vision module combining a structured laser light projector with a CID camera to monitor the weld bead geometry during grinding. Digitised weld bead profiles are fed into a grinding pass planning algorithm which maximises the use of the limited power in a pneumatic spindle. More recently, Pandiyan et al. [3] proposed a convolutional neural network based approach to detect whether the weld seam removal has been successfully completed in a robotic abrasive belt grinding process. They used an off-the-shelf DSLR camera to acquire images of the different weld seam states and then used deep learning techniques to predict the evolution of weld seam geometry throughout the process.

Programming robot paths for parts with nonconformities can be a very time-consuming task without the assistance of sensors. There have been different sensor-assisted path generation techniques proposed in the literature [4-7] mainly for deburring. Vision-based techniques appear to be more promising compared to others as they could provide the model of the as-manufactured part in which the deviations due to nonconformities can be detected quickly and in detail. The workpiece localisation is a way of using vision assistance to program the paths automatically or alternatively set a datum frame at a relevant point on the part which can be used to alter pre-defined paths. Mathematical aspects of the workpiece localisation were discussed in detail by Zexiang et al. [8]. Rajaraman et al. [9] extracted edge features from parts with a rough, pre-determined position, using a laser line scanner, and matched them with CAD models in order to localise a part in two dimensions. A study by Kosler et al. [10] took scans of a reference part, which were compared with scans taken of new workpieces using the Iterative Closest Point (ICP) algorithm, in order to transform and fit a pre-programmed tool path. Posada et al. [7] used a calibrated laser scanner to obtain 3D point cloud data, based on the known kinematics of a robot. They also used the ICP method, to match 3D data from a calibrated laser scanner to a nominal CAD model for localisation, and for looking ahead of the tool during a machining operation, in order to compensate for any geometrical deviations.

The aim of this paper is to present a milling-based robotic finishing system to remove FSW marks and flash from the part using vision assistance. It was developed considering the process requirements of the example component in Fig. 1. However, its application is not limited to the given example only and could be suitable to any prismatic component. In contrast to the methods discussed above, this paper aims to present an industry-focused approach, with reference to the results of machining operations, and a discussion of how to select machining parameters, based on stability analysis.

The paper is organised as follows. The theoretical foundations of the system features are described in details in Section 2. Results of the cutting trials to demonstrate the system on an industry-scale component are presented in Section 3. Conclusions of the study and additional discussions are given in Section 4.

2. Vision-assisted robotic finishing system

The developed robotic finishing system is based on the concept of scanning and machining with the same end effector as shown in Fig. 2 (a). The robot in the system is a factory-calibrated 6-axis Stäubli TX200 robot with ±0.06 mm repeatability. A line structured laser sensor, Micro Epsilon 2911-100/BL, is mounted on one end of the end effector adapter to scan the region to be machined as illustrated in Fig. 2 (b). It has a measurement range of 100 mm in axial and lateral directions and a resolution of 12 µm with a maximum scanning frequency of 300 Hz. A 16000 RPM pneumatic spindle with adjustable deflection unit, BIAX RSC-16000, is attached to the other end of the end effector adapter to de-flash the edges and clean up the surface as shown in Fig. 2 (c).

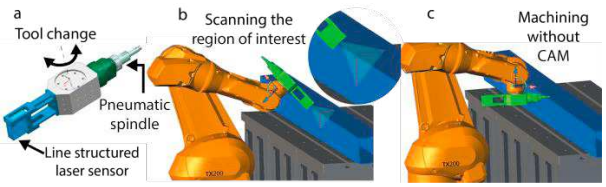

Fig. 2. (a) Vision-assisted finishing end effector. (b) Robot during scanning (c) Robot during machining.

A LabVIEW-based data acquisition and process planning interface communicates with the CS8C HP robot controller through TCP/IP protocol and it is able to exchange and alter VAL3 programs and data types online. It is connected to the laser sensor with TCP/IP also. The part can be scanned either in manual mode by the operator or in automatic mode by running an offline generated path with respect to a set or fixed datum frame. A 3D point cloud of the region of interest, which is in this case the corner joints, can be generated given the position of the flange frame during the scan and laser sensor profile coordinates which are both acquired and processed by the LabVIEW interface. Based on the maximum height of the detected flash or burr, a set of path points can be computed with respect to the robot base. Process parameters are either suggested from the lookup data embedded in the system or entered by the operator. Once the path is generated and checked by the operator, the spindle is selected by rotating the flange

180 degrees, and the machining operation begins. The process is presented in detail in the following sections.

2.1. Workpiece localisation

The localisation of the workpiece in the robot base coordinate system – or simply robot base frame – is the first and essential step of the presented robotic machining system as it enables automatic generation of the machining path later on. For localisation with the laser sensor, the kinematic relationship between the laser frame and base frame has to be known. Illustrated in Fig. 3, the problem of defining this relationship is known as the hand-eye calibration that aims to estimate the homogenous transformation matrix between the robot base frame and wrist-mounted sensor frame.

Suppose that $P_L = [x_L, y_L, z_L, 1]^T$ is a point read by the laser sensor on an object fixed in the robot base frame, T is the transformation matrix between the base frame and flange frame and X is the transformation matrix between the flange frame and laser frame, the hand-eye calibration problem can be formulated, as described in [11], as follows:

$$T_1 X P_{L_1} = T_2 X P_{L_2} \tag{1}$$

where indices *1* and *2* specify the initial and final poses of the robot. X is a 4 x 4 homogenous transformation matrix between the flange frame and laser frame assumed to be the only unknown in the Eq. (1) and remains constant in the initial and final poses of the robot, provided that the laser is rigidly mounted. Pre-multiplying both sides by T_2^{-1} and then post-multiplying by $(P_{L1})^{-1}$, Eq. (1) can be written in an alternative form as below:

$$AX = XB \tag{2}$$

where $A = T_2^{-1} T_1$ and $B = P_{L_2} P_{L_1}^{-1}$. There have been different methods proposed in the literature [12-14] to solve the $AX = XB$ equation for X. One of the methods, which could be considered as practical especially in an industrial environment, is referred to as two-stage solution which decomposes the equation into two parts and solves both parts consecutively.

When P_L is measured in the laser sensor frame, it can be transformed into the base frame as follows:

$$\begin{bmatrix} P_B \\ 1 \end{bmatrix} = \begin{bmatrix} R & t \\ 0 & 1 \end{bmatrix} \begin{bmatrix} R_L & t_L \\ 0 & 1 \end{bmatrix} \begin{bmatrix} P_L \\ 1 \end{bmatrix} \tag{3}$$

where P_B is the measured point transformed into the base frame, R and t are the rotation and translation parts of the homogenous transformation matrix T between the flange frame and base frame and $\boldsymbol{R_L}$ and $\boldsymbol{t_L}$ are the rotation and translation parts of the homogenous transformation matrix X between the laser frame and flange frame, which are the unknowns and written in bold in this paper for readability. For two consecutive robot poses n-1 and n, Eq. (3) can be expanded as below:

$$R^{n-1} \cdot R_L^{n-1} \cdot P_L^{n-1} + R^{n-1} \cdot t_L^{n-1} + t^{n-1} = R^n \cdot R_L^n \cdot P_L^n + R^n \cdot t_L^n + t^n \tag{4}$$

From Eq. (4), R_L and t_L can be estimated through a set of laser sensor measurements of a target point fixed in space. A common target point which could be used in this process is the centre of a calibration sphere with a known diameter.

In the first step of the two-stage solution, $\boldsymbol{R_L}$ should be estimated first as the second step requires $\boldsymbol{R_L}$ to be available. If the centre point of a sphere, P_L is measured by the laser sensor in two consecutive robot poses in a way that the flange frame orientation would remain unchanged, namely $R^n = R^{n-1}$, then Eq. (4) is simplified to:

$$\boldsymbol{R_L} \cdot [P_L^{n-1} - P_L^n] = \left(R^n\right)^{-1} \cdot [t^n - t^{n-1}] \tag{5}$$

For i measurements of the sphere centre while $R^n = R^{n-1}$ in each measurement, a system of linear equations can be obtained as:

$$\begin{aligned} &\boldsymbol{R_L} \cdot M = N, \\ &M = \left[P_L^1 - P_L^2, P_L^2 - P_L^3, \ldots, P_L^{n-1} - P_L^n \right], \\ &N = [(R^n)^{-1} \cdot (t^2 - t^1), \ldots, (R^n)^{-1} \cdot (t^n - t^{n-1})] \end{aligned} \tag{6}$$

where M and N are 3 x i and $\boldsymbol{R_L}$ is 3 x 3 matrices.

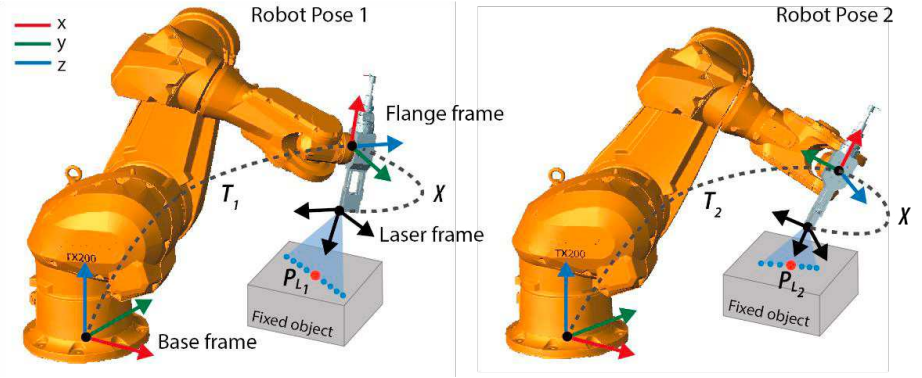

Fig. 3. Description of the hand-eye calibration problem for the Stäubli TX200 and laser sensor.

The singular value decomposition of MN^T gives its left and right singular matrices U and V which can then be used to calculate $\boldsymbol{R_L}$ as:

$$\boldsymbol{R_L} = V \cdot U^T \tag{7}$$

In the second step of the solution, similar to the first one, the centre of the sphere P_L is measured by the laser sensor again in two consecutive poses in which, this time, the flange frame position remains unchanged to reduce Eq. (4) to:

$$\left[R^{n-1} - R^n\right] \cdot \boldsymbol{t_L} = \left[R^n \cdot \boldsymbol{R_L} \cdot P_L^{\,n} - R^{n-1} \cdot \boldsymbol{R_L} \cdot P_L^{\,n-1}\right] \tag{8}$$

Taking k consecutive measurements of the sphere centre while $t^n = t^{n-1}$ and plugging $\boldsymbol{R_L}$ in, $\boldsymbol{t_L}$ can be found by solving Eq. (8) through least-squares estimation. A series of experiments were carried out to estimate $\boldsymbol{R_L}$ and $\boldsymbol{t_L}$ of the laser sensor as shown in Fig. 4 (a) and validate the described calibration method. The calibration object used in the experiments was a 30 mm diameter calibration sphere (R_s = 15 mm) coated with a matt layer to minimise the effect of reflection. In all experiments, the aim was to locate the centre of the sphere (x_L, y_L, z_L) in different robot poses. Therefore, the laser sensor was pointed at the sphere at a given robot pose and the intersection of the sphere surface and laser plane, which would be a near-perfect circle neglecting the inherent noise in the instrumentation, was acquired. Each measurement consisted of a 1280 x 2 data set, meaning that the x (lateral) and z (depth) components of 1280 points were taken, representing 2D coordinates of the sphere-laser light intersection in the laser frame. For each acquired data set, the centre (x_L, z_L) and radius (R_c) of the sphere-laser plane intersection were calculated by circle fitting as illustrated in Fig. 4 (b). The third coordinate of the sphere centre y_L was found using the Pythagorean theorem. It should be noted that the sign of y_L can take a positive or negative value according to the position of the sphere centre in the laser frame. 6 and 10 measurements were taken respectively, each containing a data set in the initial and final poses of the robot as required by the calibration method, to estimate $\boldsymbol{R_L}$ and $\boldsymbol{t_L}$ solving Eq. (5) and Eq. (8), respectively.

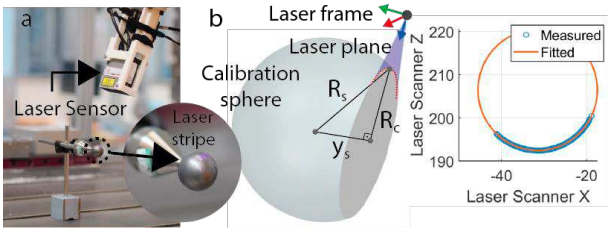

Fig. 4. (a) Laser sensor measurements on the calibration sphere. (b) Calculation of the sphere centre.

Once the calibration process was completed, the sphere was partly scanned in 3 different robot poses for validation. The centre point and radius of each validation data set were calculated through least-squares estimation. Presented in Table 1 and Fig. 5, results show that it is possible to achieve submillimetre accuracy in the workpiece localisation with a very small number calibration data set. The standard deviation for y_L, z_L and R_s is less than 0.5 mm whereas it is relatively higher for x_L being around 0.8 mm, which are a comparable order of magnitude with the results obtained in [14] with similar number of measurements.

Table 1. Results of calibration validation trials presented in the robot base frame.

Measurement	x_L (mm)	y_L (mm)	z_L (mm)	R_s (mm)
Sphere 1	1034.532	662.340	298.366	15.391
Sphere 2	1033.544	661.356	297.513	15.195
Sphere 3	1032.899	661.929	297.913	15.157
Standard Deviation	0.822	0.494	0.427	0.125

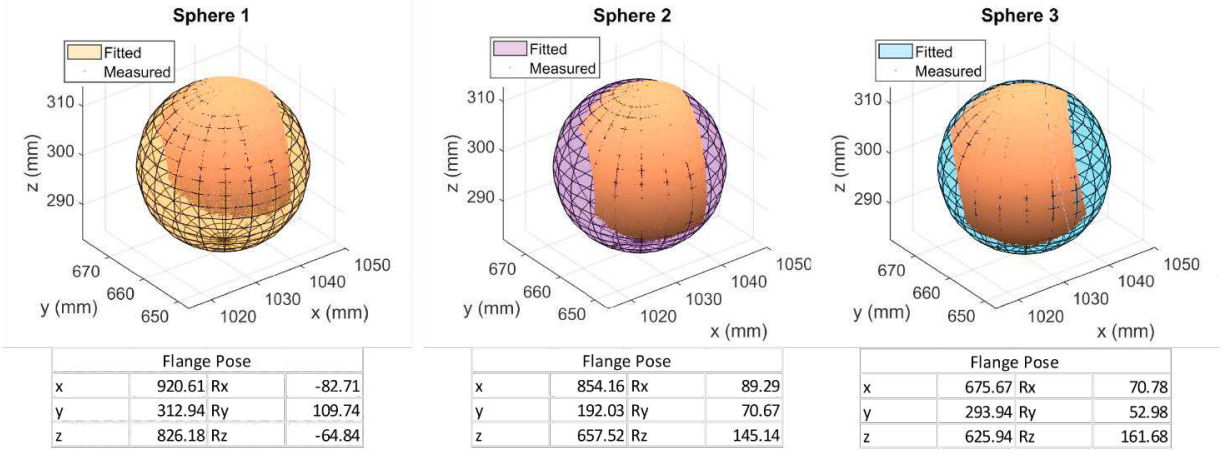

Fig. 5. Calibration validation trials at 3 different robot poses.

2.2. Automatic Path Generation

An industrial robot path consists of a sequence of frames describing the desired poses of the tool frame during the motion. Once the workpiece reconstruction and localisation by scanning have been completed with a sufficient accuracy, a set of reference geometrical features can be defined on the scan model of the workpiece which will enable path frames to be computed automatically. The first step of this procedure is to filter the scan data to remove the noise caused by the laser reflection especially from the corner flash. Depending on the severity of the noise, 3rd or 5th order one-dimensional median filtering along the scanning direction can eliminate the outliers without smoothing the data excessively. The second step is to calculate the total depth of material to be removed from the top surface. Shown in Fig. 6 (a), as the top and side faces of the corner joint are planar, they can be set as datum planes and taken as reference for the calculation of the total depth.

Suppose that P_t and P_s are two planes fitted to a series of points on the top and side surfaces of the corner joint whereas $\vec{n}_t$ and $\vec{n}_s$ are the unit normal vectors and q_{tc} and q_{sc} are the centroids of these two planes, respectively. Let p_{fmax} be a point on the corner joint where the height of the flash is maximum with respect to P_t. Assume that d and w are scalars for the maximum depth and width of the FSW tool marks, respectively. In this case, the total depth to be removed from the corner joint, z, can be expressed as:

$$z = d + \left| (p_{f\max} - q_{tc}) \cdot n_t \right| \tag{9}$$

The third step is to calculate the tool orientation which is assumed to remain constant during machining as the corner joint does not have any curvature. As shown in Fig. 6 (b), planes P_t and P_s intersect along a line where $\vec{v}_l$ is the unit direction vector of the line which can be found by taking the cross product of $\vec{n}_t$ and $\vec{n}_s$. Ideally, $\vec{n}_t$, $\vec{n}_s$ and $\vec{v}_l$ are expected to be orthogonal to each other meaning that they would construct a rotation matrix which would define the tool orientation during machining. However, due to the errors caused by plane-fitting and rounding, the constructed rotation matrix may have a determinant different from, although close to, 1 and therefore it is required to be orthogonalised. After the orthogonalisation, the rotation matrix is decomposed into Euler angles which define the tool orientation.

The fourth step is to locate the points which define the frame origins in the machining path. Plane-fitting to the first and last profiles in the scan data, the corner joint is bounded by two planes, P_{en} and P_{ex}, which indicate the tool's entry and exit planes, respectively. The intersection of these two planes with the unit direction vector, $\vec{v}_l$, results in two sets of points on the part. Offsetting these points in the direction of $\vec{n}_t$ and $\vec{n}_s$ by z and w will yield the starting and ending points of the first path segment which can be found by linear interpolation. If the tool frame is defined at the centre of the tool, the diameter compensation should also be taken into account. Dividing z to the desired radial depth of cut, a_e, the number of passes can be calculated which will enable to locate the rest of the segments by offsetting.

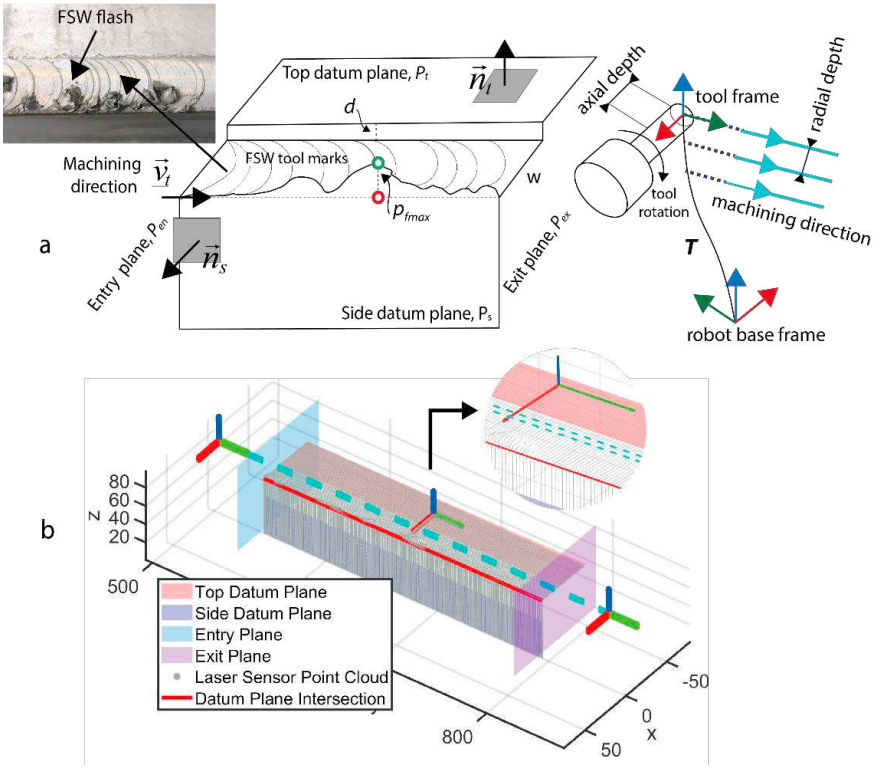

Fig. 6. (a) FSW joint geometry and description of variables. (b) Generated path on the scan data

2.3. Selection of Cutting Parameters

There are several types of cutting tools that could be suitable for the machining task described in Fig. 6 (a), including abrasive discs, mounted points, carbide round tools and so on. In comparison to mounted points or similar abrasives, carbide round tools are able to remove more material and yield longer tool life when finishing FSW surfaces of softer materials and therefore are preferred where possible. However, in the case of carbide round tools such as end-mills and burrs, larger widths of FSW marks which are typically between 15 mm and 40 mm, require longer tool stick-out lengths which increases the risk of chatter. In order to mitigate this risk, the spindle speed and axial depth or radial depth combination should be selected considering the dynamics of the robot-spindle-tool system.

One of the most commonly used spindle types for robotic finishing is air-driven pneumatic spindle which works as an open-loop system meaning that setting and control of the spindle speed is not practical. In this case, axial and radial depth appear to be the only cutting parameters that can be actually controlled against chatter. Described in detail in [15], the process of selecting these two parameters begins with determining the tool-tip frequency response function (FRF) through modal testing. Tool-tip FRF can then be used to simulate the process stability, in this case milling with carbide round tools, for a set of cutting conditions.

One way of displaying the output of these simulations is the stability lobe diagram which plots the stable axial or radial depth against the spindle speed. In every stability lobe diagram, there is an absolute stability limit below which the process is considered to be stable for any axial or radial depth regardless of the spindle speed. For chatter-free robotic finishing with carbide round tools, it is proposed that the absolute stability limit would be used to determine the axial and radial depth combination.

To illustrate, Fig. 7 (a) shows the results of a series of impact tests conducted at the tip of a 6 mm diameter and 4 flutes carbide end-mill inserted into a pneumatic spindle attached to the end effector previously shown in (a). The tests were carried out using 3 sizes of impact hammers to acquire the FRF in a wider spectrum. Fig. 7 (b) shows the results of stability analyses carried out to find the chatter-free axial and radial depth combination.

Embedding this data into the process planning interface in the form of a graph or look-up table, cutting parameters can be selected correctly minimizing the risk of chatter.

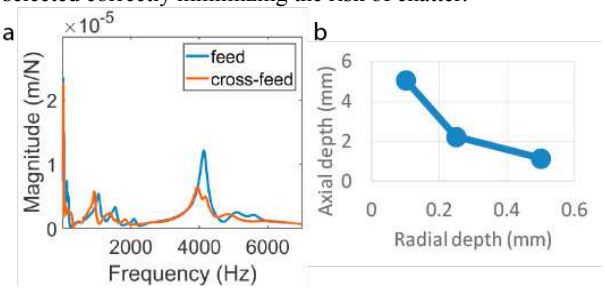

Fig. 7. (a) Tool tip FRF of 6 mm diameter and 27 mm stick-out end mill. (b) Axial and radial depth selection based on the absolute stability.

3. Cutting Trials

In order to demonstrate the developed robotic finishing system, cutting trials were carried out with a 6 mm diameter, 45 degrees helix angle and 4 flutes carbide end-mill tightened into the spindle with an ER collet. The part was a 250 mm x 250 mm x 1070 mm friction stir-welded borated aluminium tube securely clamped down to the machining bed. In the first step, one corner-joint was scanned along its length at 25 mm/s robot feed. In the second step, the part was machined at 60 mm/s robot feed to a smooth surface finish. Spindle speed varied in the trials between 7200 RPM and 8400 RPM. The axial and radial depths were selected using the graph given in Fig. 7 (b). The description of the experimental setup and involved processes are illustrated in Fig. 8.

Surface roughness measurements at 10 randomly selected points were taken along the feed direction. The process was repeated for the second corner joint to evaluate whether the results would be consistent. Fig. 9 (a) illustrates that the generated surface is fully clean and free of any FSW marks. Shown in Fig. 9 (b), it is possible to achieve around 1.1 µm average surface roughness value with the described method. In addition, from Fig. 9 (c) the deviation of the average surface roughness between two machined corners is also negligibly small which points out that the developed weld finishing process is repeatable from the quality perspective.

Fig. 8. The description of the vision-assisted robotic finishing setup and process flow.

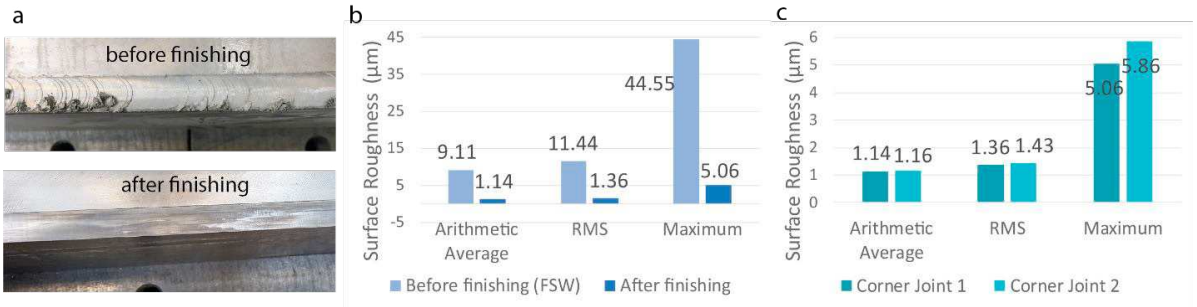

Fig. 9. (a) Surface picture before and after. (b) Surface roughness before and after. (c) Process repeatability in surface roughness results.

4. Conclusion

A robotic finishing system with the scan-and-machine approach is presented. The system combines the workpiece localisation, automatic path programming and process parameter selection features, coordinated by a LabVIEW VI, which is in communication with the robot controller at all times. It has been shown that the workpiece can be localised in the robot base frame using a range of robot pose configurations, with a maximum standard deviation in the scanned coordinates of 0.82 mm. It is expected that increasing the number of calibration data and enlarging the calibration workspace would significantly improve the localisation accuracy, reducing the well-known contribution of joint errors (e.g. gear backlash, encoder error) to positional inaccuracy across the range of possible robot poses. Automatic path generation on the reconstructed 3D point cloud is promising because it eliminates the CAM and verification process. However, additional supervision may be required to avoid collision risks. Cutting tests have demonstrated that the developed robotic finish machining system is able to achieve average surface roughness values of approximately 1.1 µm in the removal of friction-stir welding excess material, with a high repeatability. This meets the required surface quality set by the industry-standards which, for the finished part, is around 1.25 µm. The system is also a cost-effective solution as it does not have to be equipped with expensive laser tracking or tool changing equipment which may cost, in total, more than the robot itself.

Acknowledgements

The authors would like thank Fernando Sanchez Oruña from the Equipos Nucleares S.A. for their support on the carried out work and acknowledge the funding provided by the European Commission under the Horizon 2020 Programme to the COROMA project under the grant agreement no.723853.

References

[1] N.Z. Khan, A.N. Siddiquee, Z.A. Khan, Friction Stir Welding of Aluminum Alloys, Friction Stir Welding 6608 (2017) 71–98.
[2] D.E. Whitney, A.C. Edsall, A.B. Todtenkopf, T.R. Kurfess, A.R. Tate, Development and Control of an Automated Robotic Weld Bead Grinding System, Journal of Dynamic Systems, Measurement, and Control 112 (1990) 166.
[3] V. Pandiyan, P. Murugan, T. Tjahjowidodo, W. Caesarendra, O.M. Manyar, D.J.H. Then, In-process virtual verification of weld seam removal in robotic abrasive belt grinding process using deep learning, Robotics and Computer-Integrated Manufacturing 57 (2019) 477–487.
[4] H. Zhang, H. Chen, N. Xi, Automated robot programming based on sensor fusion, Industrial Robot 33 (2006) 451–459.
[5] G. Seliger, L.H. Hsieh, G. Spur, Sensor-Aided Programming and Movement Adaptation for Robot-Guided Deburring of Castings, CIRP Annals - Manufacturing Technology 40 (1991) 487–490.
[6] A. Kuss, M. Drust, A. Verl, Detection of Workpiece Shape Deviations for Tool Path Adaptation in Robotic Deburring Systems, Procedia CIRP 57 (2016) 545–550.
[7] J. Ricardo, D. Posada, S. Kumar, A. Kuss, U. Schneider, M. Drust, T. Dietz, A. Verl, Automatic Programming and Control for Robotic Deburring Description of the Robot Deburring System, ISR 2016 (June 21 – 22, 2016, Munich, Germany) Automatic 2016 (2016) 688–695.
[8] Zexiang Li, Jianbo Gou, Yunxian Chu, Geometric algorithms for workpiece localization, IEEE Transactions on Robotics and Automation 14 (1998) 864–878.
[9] M. Rajaraman, M. Dawson-Haggerty, K. Shimada, D. Bourne, Automated workpiece localization for robotic welding, IEEE International Conference on Automation Science and Engineering (2013) 681–686.
[10] H. Kosler, U. Pavlovčič, M. Jezeršek, J. Možina, Adaptive Robotic Deburring of Die-Cast Parts with Position and Orientation Measurements Using a 3D Laser-Triangulation Sensor, Strojniski Vestnik/Journal of Mechanical Engineering 62 (2016) 207–212.
[11] Y. Shiu, S. Ahmad, Calibration of Wrist-Mounted Robotic Sensors by Solving Homogeneous Transformation Equations of the Form AX=XB, IEEE Transactions On Robotics And Automation, 5(1) (1989) 16-29
[12] G.B. de Sousa, A. Olabi, J. Palos, O. Gibaru, 3D Metrology Using a Collaborative Robot with a Laser Triangulation Sensor, Procedia Manufacturing 11 (2017) 132–140.
[13] S. Yin, Y. Guo, Y. Ren, J. Zhu, S. Yang, S. Ye, A novel TCF calibration method for robotic visual measurement system, Optik 125 (2014) 6920–6925.
[14] S.R. Fernandez, A. Olabi, O. Gibaru, Proceedings of 2018 IEEE 3rd Advanced Information Technology, On-line Accurate 3D Positioning Solution for Robotic Large-Scale Assembly Using a Vision System and a 6dof Tracking Unit, Electronic and Automation Control Conference, IAEAC 2018 (2018) 682–688.
[15] Y. Altintas, E. Budak, Analytical Prediction of Stability Lobes in Milling. CIRP Annals, 44(1) (1995) 357–362.